Proceedings of the
Annual Stability Conference
Structural Stability Research Council
Atlanta, Georgia, April 21-24, 2020

An assessment of the Eurocode 3 provisions for lateral-torsional buckling of I-sections under uniaxial and biaxial bending

Rodrigo Gonçalves[1]

Abstract
In this paper, a two-node geometrically exact beam finite element developed by the author (Gonçalves 2019), which is capable of accounting for Wagner effects, plasticity, geometric imperfections and residual stresses, is employed to assess the current Eurocode 3 (CEN 2005) provisions for I-section beams susceptible to lateral-torsional buckling and subjected to uniaxial or biaxial bending. For uniaxial bending, three support/loading cases are considered: (i) simply supported beams under uniform moment, (ii) simply supported beams subjected to a mid-span vertical force and (iii) cantilevers subjected to a free end vertical force. Besides I-sections with standard height-to-width ratios, wider flange sections are also considered and it is shown that the post-buckling behavior of the latter sections is quite different from that of the former ones, exhibiting an increase in the load carrying capacity which is not predicted by Eurocode 3. For biaxial bending, a standard I section is considered and three support/loading cases are examined: (i) simply supported beams under uniform moments, (ii) beams simply supported at one end and fixed at the other, subjected to end moments, and (iii) cantilevers subjected to free end forces. For these loadings, it is shown that the Eurocode 3 Method 2 interaction formulas can lead to very inaccurate estimates of the collapse load, either on the conservative or unconservative side.

1. Introduction
According to the current Eurocode 3 (CEN 2005), for beams susceptible to lateral-torsional (LT) buckling, the following equation must be satisfied

$$\frac{M_{y,Ed}}{\chi_{LT} M_{y,Rk}/\gamma_{M1}} \leq 1, \tag{1}$$

where
$M_{y,Ed}$ is the design value of the maximum moment acting in the beam, along the strong axis (y), $M_{y,Rk}$ is the cross-section characteristic moment resistance about the same axis, γ_{M1} is the partial factor for resistance of members to instability assessed by member checks (the recommended value is $\gamma_{M1} = 1.0$) and χ_{LT} is the reduction factor for LT buckling. This reduction factor is obtained

[1] Associate Professor, CERIS and Universidade Nova de Lisboa, Portugal, <rodrigo.goncalves@fct.unl.pt>

from the appropriate buckling curve in the code and the LT slenderness is given by $\bar{\lambda}_{LT} = \sqrt{M_{y,Rk}/M_{cr}}$, where M_{cr} is the critical buckling moment, obtained from a standard linear stability analysis. In the current Eurocode 3 (EC3) version, two methods are provided for the calculation of the reduction factor: (i) the "general case" (GC) of clause 6.3.2.2 and (ii) the "special case" (SC) of clause 6.3.2.3, which applies to rolled I-sections or equivalent welded sections. For the SC, it is possible to modify (increase) the reduction factor obtained from the buckling curves through $\chi_{LT,mod} = \chi_{LT}/f \leq 1$, where the modification factor f (with $f \leq 1$) is a function of the slenderness and the shape of the bending moment diagram between lateral restraints (the maximum value equals $f = 1$ and corresponds a uniform moment diagram).

Short after the publication of the current EC3 provisions, several studies assessing the new LT rules have been presented (see, e.g., Snijder & Hoenderkamp 2007, Rebelo et al. 2009), showing that in some cases fairly large discrepancies between numerical and code resistance values are obtained. This led to the proposal of new LT rules for standard sections (e.g., Taras & Greiner 2010, Kucuckler et al. 2015, Snijder et al. 2018). All these studies involved parametric studies based on geometrically and materially non-linear numerical analyses, including geometric imperfections and residual stresses (usually designated as "GMNIA"), using refined shell finite element models, even for compact cross-sections (see also Snijder et al. 2008, Taras 2016). However, if local/distortional buckling is not relevant, beam (one-dimensional) finite elements constitute an attractive choice, as they provide sufficiently accurate results with a much lower computational cost and, moreover, deal directly with cross-section stress resultants, which are of interest for designers.

This paper discusses results concerning the application of the current EC3 provisions for compact I-section beams undergoing lateral-torsional buckling and subjected to uniaxial (Section 3) or biaxial bending (Section 4). For uniaxial bending, besides I-sections with standard height-to-width ratios, wider flange sections are also considered and it is shown that, for the latter, the collapse loads can be much higher than those provided by the EC3 buckling curves. For biaxial bending, a standard I section is considered and it is demonstrated that the so-called "Method 2" of EC3 can provide very inaccurate collapse load estimates (either on the conservative or unconservative side). All the non-linear analyses are carried out with a two-node geometrically exact beam finite element developed by the author (Gonçalves 2019), which includes plasticity, geometric imperfections and residual stresses. This element is briefly described in Section 2. Finally, Section 4 presents the concluding remarks.

2. Some notes concerning the beam finite element employed

The details of the beam element used to obtain the results presented in this paper are provided in Gonçalves (2016, 2019). The element is based on the so-called "geometrically exact beam theory", pioneered by Reissner (1972) and Simo (1985), which is based on a kinematic description of the cross-section that involves a translation and a true (finite) rotation. The theory has been continuously improved to include cross-section deformation, namely torsion-related warping (Simo & Vu-Quoc 1991, Gruttmann et al. 2000, Atluri et al. 2001) and many other effects — an application to thin-walled deformable cross-sections and a list of other relevant developments is provided in Gonçalves et al. (2010).

The present element has two nodes and includes torsion-related warping, leading to 7 DOFs per node. Wagner effects are included without simplifications, since all terms of the Green-Lagrange strains are retained. Reduced (one point) integration along the element length is carried out, to avoid locking. The element can account for plasticity and residual stresses. The finite element procedure was implemented in MATLAB (2010), with a load/displacement control strategy.

In all the analyses carried out in this work, the beams are discretized with 30 equal length finite elements. For the GNIAs (geometric non-linear analyses with imperfections), 3/2 Gauss points are considered in each cross-section wall, along the mid-line and through-thickness directions, respectively, and the geometric imperfection has the form of a lateral half-wave sinusoid, with amplitude e_0. For the GMNIAs (geometric and material non-linear analyses with imperfections), an elastic-perfectly plastic material law is employed, with yield stress $f_y = 235$ MPa and 11/3 Gauss points in each wall (mid-line/through-thickness directions), to capture the spreading of plasticity accurately. The imperfection amplitude equals $e_0 = L/1000$ and the residual stress pattern considered is displayed in Fig. 1.

It should be mentioned that, although the load-displacement curves presented in this paper are calculated up to large displacements, in some cases these equilibrium paths are not realistic, as local buckling is eventually triggered (an effect not captured by the beam finite element) and/or serviceability governs. However, these curves are provided because their shape is essential to help understanding the non-linear behavior of the beams.

3. Lateral-torsional buckling under uniaxial bending

This section addresses the LT buckling behavior of steel I-section beams with three support/loading cases:

Case 1 – simply supported beams (standard "fork" supports) under uniform bending;

Case 2 – simply supported beams acted by a vertical force, applied at the mid-span cross-section shear centre;

Case 3 – cantilevers acted by a vertical force, applied at the free end cross-section shear centre.

Four cross-sections are considered (see Fig. 1). According to the EC3 cross-section classification, sections C1, C3 and C4 are class 1 (local buckling does not affect the formation of a plastic hinge with a rotation capacity required in a plastic analysis) and section C2 has a class 2 flange (may develop its full plastic moment but has limited rotation capacity). These cross-sections were

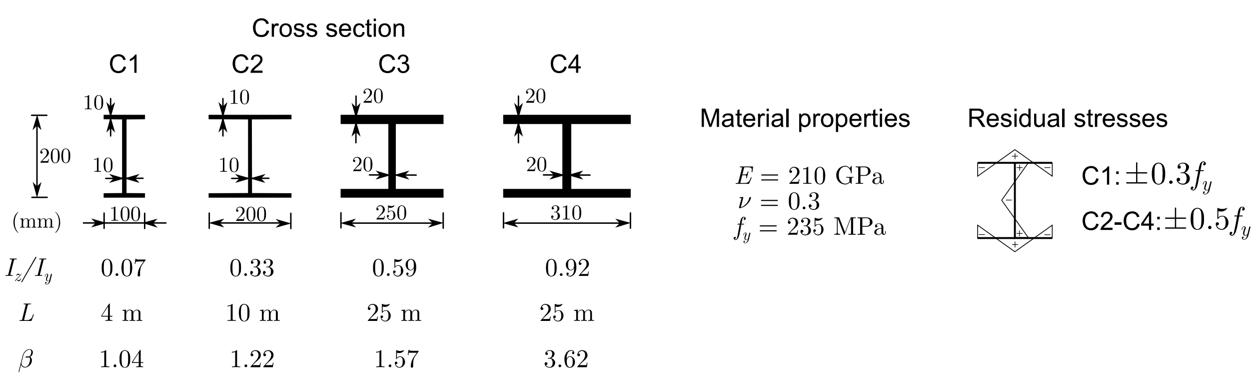

Figure 1: Cross-section geometries, material properties and residual stresses adopted for the uniaxial bending cases

chosen based on their height-to-width and weak-to-strong axes second moments of area (I_z/I_y) ratios: C1 and C2 have standard ratios, whereas sections C3 and C4 are non-standard — in particular, $I_z/I_y \approx 1$ for section C4.

Fig. 1 also provides the values of the parameter (Pi & Trahair 1992)

$$\beta = \frac{M_{cr}^{NSA}}{M_{cr}^{LSA}} \frac{1}{\sqrt{\left(1-\frac{I_z}{I_y}\right)\left(1-\left(GJ+\frac{\pi^2 EI_\omega}{L^2}\right)/2EI_y\right)}}, \tag{2}$$

where the superscripts *NSA* and *LSA* designate "non-linear" and "linear" stability analyses, respectively (the former takes into account pre-buckling deflections), J is the St. Venant torsion constant, I_ω is the warping constant and L is the beam length (the values adopted are also provided in the figure).

For I sections, Eq. (2) essentially depends on the I_z/I_y ratio. As this ratio increases, β increases and the difference between the *NSA* and *LSA* critical moment also increases (note that one obtains $\beta = \infty$ for $I_z = I_y$). Although this equation was derived for simply supported beams (standard "fork" supports) subjected to uniform bending, using several simplifying assumptions, such as small rotations, small strains and moderate deflections, it is shown in the present paper that it may be used to estimate M_{cr}^{NSA} for large pre-buckling displacements and other loading/support cases.

2.1 Case 1: simply supported beams under uniform bending

The graphs in Fig. 2 plot the GNIA and GMNIA load-displacement curves obtained for Case 1 and all cross-sections (C1 to C4), for the beam lengths indicated in Table 1 (leading to $\bar{\lambda}_{LT} \approx 1.1, 1.2$). In these graphs, the vertical axis is normalized with respect to M_{cr}^{NSA} and the horizontal axis is normalized with respect to $\alpha L^2 M_{cr}^{NSA}/8EI_y$, meaning that the mid-span vertical displacement in a linear analysis equals 1 when $M = \alpha M_{cr}^{NSA}$, where $\alpha = 4$ is simply a scaling factor used to improve the visualization of the graphs. Furthermore, Table 1 shows all the relevant data, namely the beam lengths considered (as already mentioned), the slenderness values and the corresponding GMNIA/EC3 reduction factors. For the latter, buckling curves *a* and *b* are employed for the GC and SC methods, respectively (these curves will also be used for Cases 2 and 3, presented in the next subsections). These results lead to the following conclusions:

(i) The load-displacement curves in Fig. 2 show that the GNIA post-buckling stiffness increases with I_z/I_y, with quite steep paths being obtained for the non-standard sections C3 and C4. This post-buckling stiffness is most remarkable for section C4 due to the fact that, for this section, the trivial and buckled (twisted) configurations have almost the same bending stiffness.

(ii) The (negative) slopes of the GMNIA post-peak curves in Fig. 2 are somewhat related to their GNIA counterparts: for section C1 the GMNIA path has the most negative slope (its GNIA counterpart has the lowest positive stiffness) and, as the section number increases, the GMNIA paths become increasingly horizontal (their GNIA counterparts become steeper).

(iii) Although not indicated in Table 1, for all cases the finite element M_{cr}^{NSA} value falls within 0.6% of that obtained with Eq. (2) (these values are calculated by removing imperfections in

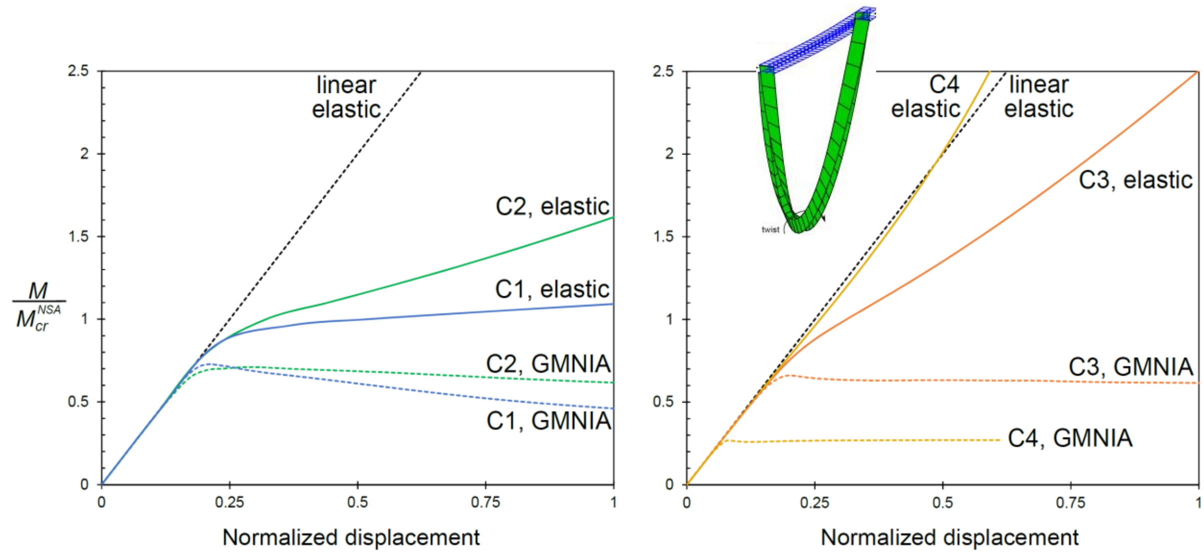

Figure 2: Uniaxial bending load-displacement plots for Case 1 and the beam lengths in Table 1

Table 1: Comparison between GMNIA and Eurocode 3 reduction factors for the uniaxial bending Case 1

Section	L (m)	$\bar{\lambda}_{LT}$	χ_{EC3}^{GC}	χ_{EC3}^{SC}	χ_{GMNIA}
C1	4	1.109	0.59	0.63	0.62
C2	10	1.234	0.51	0.56	0.56
C3	25	1.233	0.51	0.56	0.68
C4	25	1.106	0.59	0.63	0.79

the model and identifying the load at which negative eigenvalues appear in the tangent stiffness matrix). This is noteworthy, particularly for section C4, since bifurcation occurs for moderate displacements — in this case the mid-span vertical displacement equals 0.117L.

(iv) Table 1 shows that the two EC3 methods (GC and SC) yield rather different reduction factors. This difference is well-known — see, e.g., Taras & Greiner (2010).

(v) For sections C1 and C2, the SC reduction factors are very close to the GMNIA ones. This is also expected, given their standard height-to-width proportions and the residual stress pattern employed (typical for wide flange rolled sections).

(vi) For sections C3 and C4 the EC3 reduction factors are well below the GMNIA ones, particularly if the GC is employed, even though the highest buckling curves for each method were used. This difference can be attributed to their high elastic post-buckling stiffness and the fact that cross-sections with such high I_z/I_y ratios were not considered in the calibration of the EC3 buckling curves.

Since the EC3 predictions fall too much on the conservative side for the non-standard cross-sections, they are further examined by varying the member length. Fig. 3 shows the GMNIA reduction factors obtained, as a function of the slenderness (left-side graphs), and the corresponding normalized load-displacement curves (right-side graphs). The reduction factors were obtained from the first local maximum of each load-displacement curve, even though for the longer beams a higher maximum is sometimes achieved at large displacements. These graphs make it possible to conclude the following:

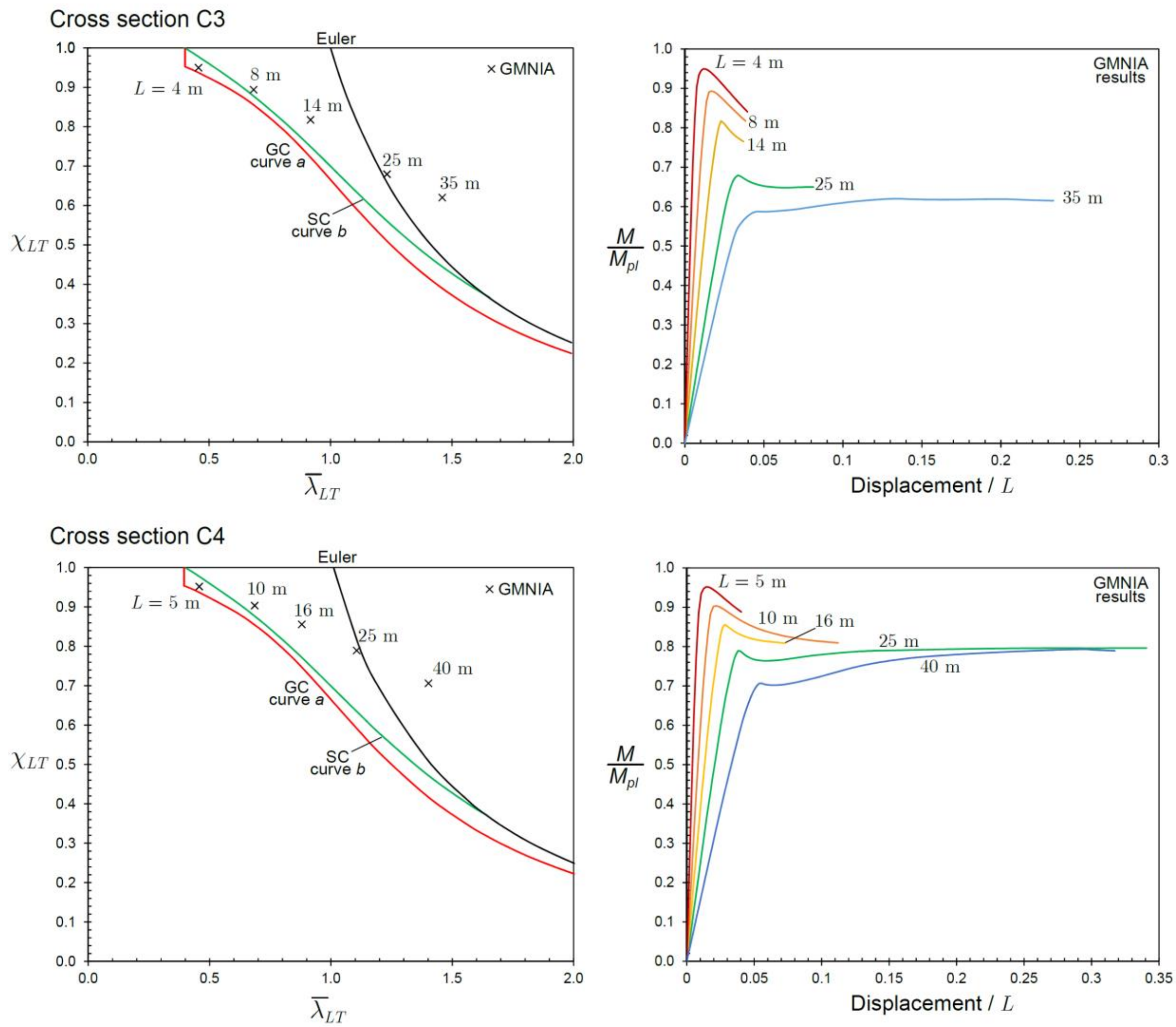

Figure 3: GMNIA results for the uniaxial bending Case 1 and C3-C4 sections with varying length: reduction factors as a function of the slenderness (left) and normalized load-displacement curves (right)

(i) A comparison between the GMNIA results and the EC3 buckling curves (left-side graphs) shows that the collapse loads are generally well above both curves, as previously concluded from the results in Table 1.

(ii) As the slenderness decreases, the GMNIA results become closer and eventually lower than the SC buckling curve. This behavior was also reported by other authors (e.g. Taras & Greiner 2010): for uniform bending, GMNIA results with $\chi_{LT} < 1$ for $\bar{\lambda}_{LT} < 0.4$ are obtained, even if strain hardening is included.

(iii) For higher $\bar{\lambda}_{LT}$ values, the GMNIA results fall above the Euler curve. This behavior was also reported for standard cross-sections by Taras (2008) and now it becomes clear that the increased load-carrying capacity is more significant as I_z/I_y increases — the reduction factors for the C4 beams are higher than for the C3 beams and recall, from Fig. 2, that the C4 beam has a much stiffer post-buckling path. However, as can be attested from the load-displacement paths (right-side graphs), this increase in the load-carrying capacity is associated with large displacements, meaning that serviceability will generally by the governing limit state. For instance, for the C3 beam with L = 25 m, in which case χ_{GMNIA} = 0.68 (and falls slightly above the Euler curve), dividing the maximum moment by 1.5 yields 109.4 kNm and corresponds to a mid-span vertical displacement of approximately L/50, which is excessive for serviceability purposes.

(iv) The right-side graphs show that, as the length increases, a post-critical capacity is observed, although it involves large displacements. It is also worth remarking that, for the cases with significant post-critical capacity, the reduction factor is virtually coincident with the weak-to-strong axis plastic bending capacity $M_{z,Rk}/M_{y,Rk}$: for section C3 this ratio equals 0.62 and, for L = 35 m, one obtains exactly $\chi_{GMNIA} = 0.62$; for section C4 one has $M_{z,Rk}/M_{y,Rk} = 0.79$ and coincides with the reduction factors obtained for L = 25 and also for L = 40 m if it is taken from the absolute maximum in the curve, rather than the first critical point. This is a consequence of the particular load case considered (uniform moment), since the beam capacity is exhausted once the mid-span cross-section twists 90º and becomes subjected to weak axis bending.

2.2 Case 2: simply supported beams under a mid-span point load

For Case 2, Fig. 4 displays the GNIA and GMNIA load-displacement curves for the beam cross-sections and lengths given in Table 2. As in Case 1, the vertical axis is normalized with respect to M_{cr}^{NSA}, but the horizontal axis is now normalized with respect to $\alpha L^3 F_{cr}^{NSA}/48EI_y$, so that the mid-span vertical displacement in a linear analysis equals 1 when $F = \alpha F_{cr}^{NSA}$ ($\alpha = 4$ is once more adopted). These curves are similar to those presented in Fig. 2 and therefore the conclusions are also similar — the GNIA post-buckling stiffness increases with I_z/I_y and this behavior is related to the corresponding GMNIA post-peak curve slope. However, it is important to note that the elastic post-buckling paths for Case 2 are stiffer than those of Case 1.

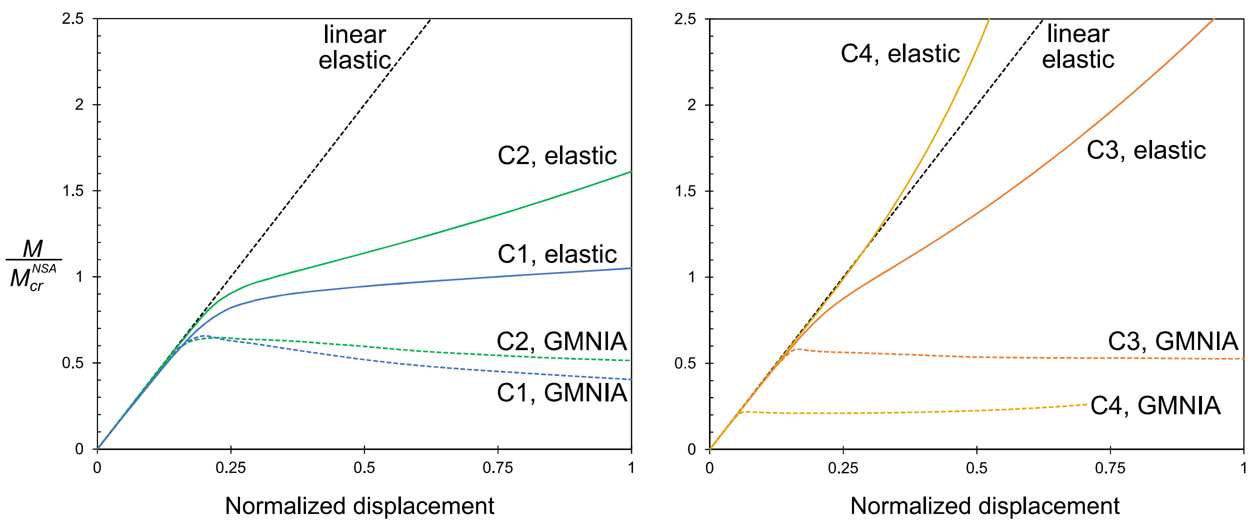

Figure 4: Uniaxial bending load-displacement plots for Case 2 and the beam lengths in Table 2

For the calculation of the EC3 reduction factors in Table 2, curves *a*/*b* were once more used for the GC/SC, respectively, and the modification factor f was employed in both methods, since it leads to higher values. Concerning the numerical β values presented in this table, a comparison with the values in Fig. 1 shows that the differences are below 2%, except for section C4, in which case 4% is obtained. This is quite remarkable, given that Eq. (2) was not developed for this load case. It is also worth noting that, for sections C1 and C2, the SC reduction factors are very close to the GMNIA ones, as expected (standard-type cross-section height-to-width ratios and residual stresses). However, for cross-sections C3 and C4, the EC3 reduction factors are once more below the GMNIA ones, particularly if the GC is employed: the $\chi_{EC3,mod}^{SC}$ values are approximately 14% below the GMNIA results, due to the high elastic post-buckling stiffness exhibited by these beams (nevertheless this difference is slightly less than that obtained for Case 1).

Table 2: Comparison between GMNIA and Eurocode 3 reduction factors for the uniaxial bending Case 2

Section	L (m)	β	$\bar{\lambda}_{LT}$	$\chi_{EC3,mod}^{GC}$	$\chi_{EC3,mod}^{SC}$	χ_{GMNIA}
C1	4	1.07	0.953	0.75	0.78	0.77
C2	10	1.23	1.061	0.66	0.70	0.71
C3	25	1.60	1.065	0.66	0.70	0.82
C4	25	3.77	0.955	0.75	0.78	0.90

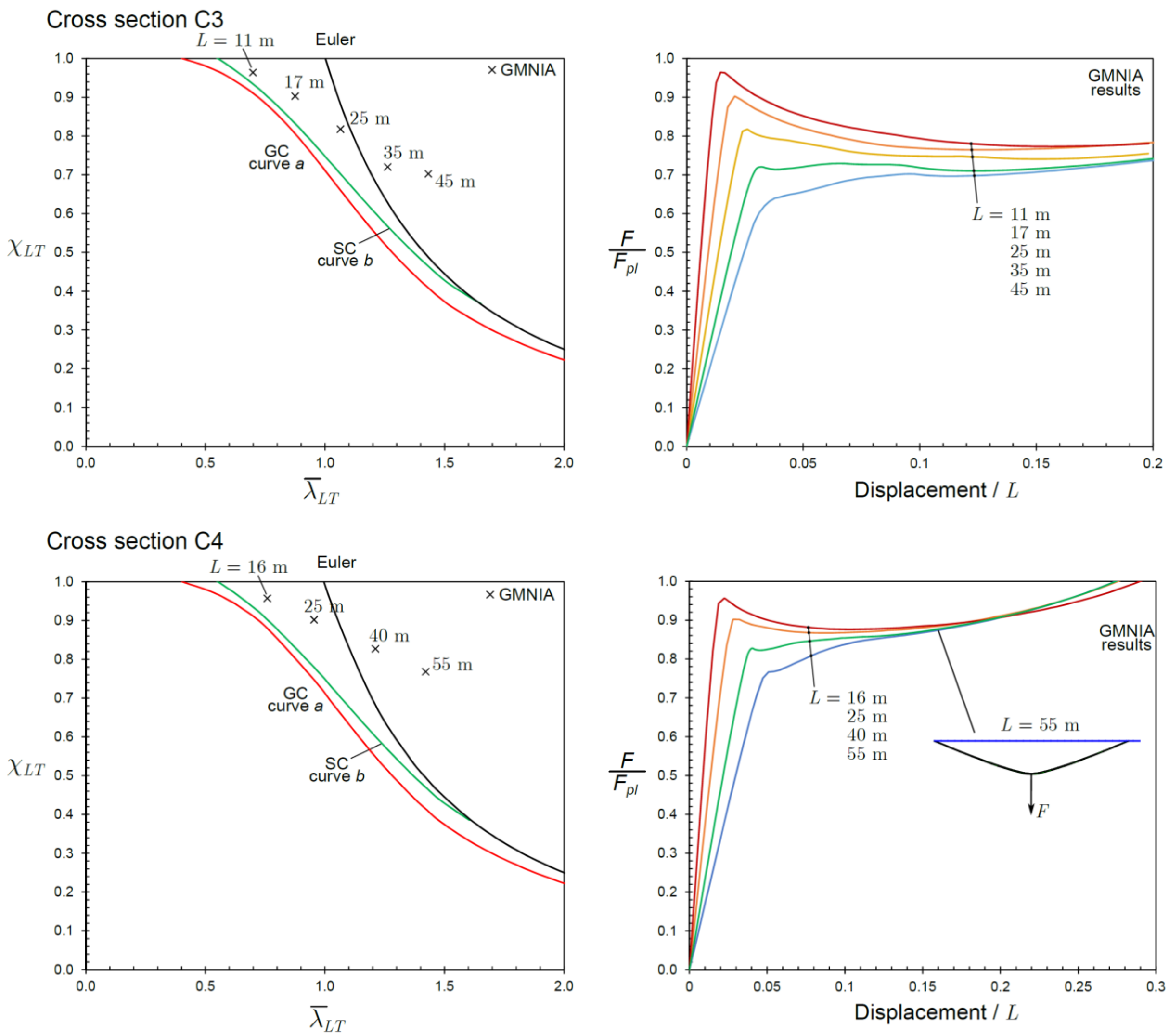

Figure 5: GMNIA results for the uniaxial bending Case 2 and C3-C4 sections with varying length: reduction factors as a function of the slenderness (left) and normalized load-displacement curves (right)

Fig. 5 shows the buckling behavior of C3 and C4 section beams when the slenderness is varied. As for Case 1, the left-side graphs show the GMNIA reduction factors, as a function of the slenderness, and the right-side graphs display the corresponding normalized load-displacement curves. Once again, the collapse loads were obtained from the first local maximum of each curve, the exception being the 55-meter span C4 beam, which does not display a maximum and thus the small horizontal plateau was considered to correspond to the collapse load. These results lead to the following conclusions:

(i) The left-side graphs show once more that the GMNIA results are well above the EC3 curves. None of the GMNIA reduction factors are lower than the SC buckling curve, which is in contrast with the results obtained for Case 1 (recall the left graphs in Fig. 3).

(ii) For the higher slenderness values, the GMNIA results fall once more above the Euler curve. This can be related to the I_z/I_y parameter, as section C4 has the highest reduction factors and simultaneously the highest elastic post-buckling stiffness. Nevertheless, the load-displacement curves reveal that the collapse load is associated with large displacements, meaning that serviceability will govern. For instance, even for the C3 beam with L = 25 m, whose GMNIA collapse load is below the Euler curve, dividing the maximum force by 1.5 yields 21.1 kN and corresponds to a mid-span displacement of approximately L/67, which is excessive for service conditions.

(iii) The right-side graphs show that, as the slenderness increases, the moment always increases after the first critical point (in contrast with the uniform moment case). This is due to a longitudinal displacement of the roller support as the load increases, causing a decrease of the maximum moment at mid-span (see the deformed configuration displayed in the bottom-right graph).

2.3 Case 3: cantilevers subjected to a free end point load

Finally, Case 3 is analyzed. The GNIA and GMNIA curves for the beam lengths displayed in Table 3 are shown in Fig. 6. As in the previous cases, the vertical axis is normalized with respect to M_{cr}^{NSA}, whereas the horizontal axis is normalized with respect to $\alpha L^3 F_{cr}^{NSA}/3EI_y$ (the free end vertical displacement in a linear analysis equals 1 when $F = \alpha F_{cr}^{NSA}$, with $\alpha = 4$). This case exhibits the stiffest elastic post-buckling responses, since the moment at the support does not increase proportionally to the loading, due to a decrease of the lever arm (i.e., due to the movement of the free end section towards the support as the beam bends). As in the previous cases, the GNIA post-buckling stiffness increases with I_z/I_y and is related to the corresponding GMNIA post-peak curve slope.

Table 3 displays once more the numerical β values, as well as the GMNIA and EC3 reduction factors. In the calculation of the EC3 values, either $f = 1$ was considered (which is in accordance with the code specifications, since both beam ends are not laterally restrained) or the value obtained assuming that the ends are restrained was adopted (although this does not comply with the code).

It is once more observed that the β parameter values in Table 3 are close to those provided in Fig. 1, although the differences are in most cases higher than those obtained for Case 2 (see Table 2). The values are within 5% of those in Fig. 1, except for section C4, in which case a 17% difference is obtained. Despite the differences reported, it can be still argued that, for this particular case, Eq. (2) can be used to estimate the critical load accounting for pre-buckling deflections.

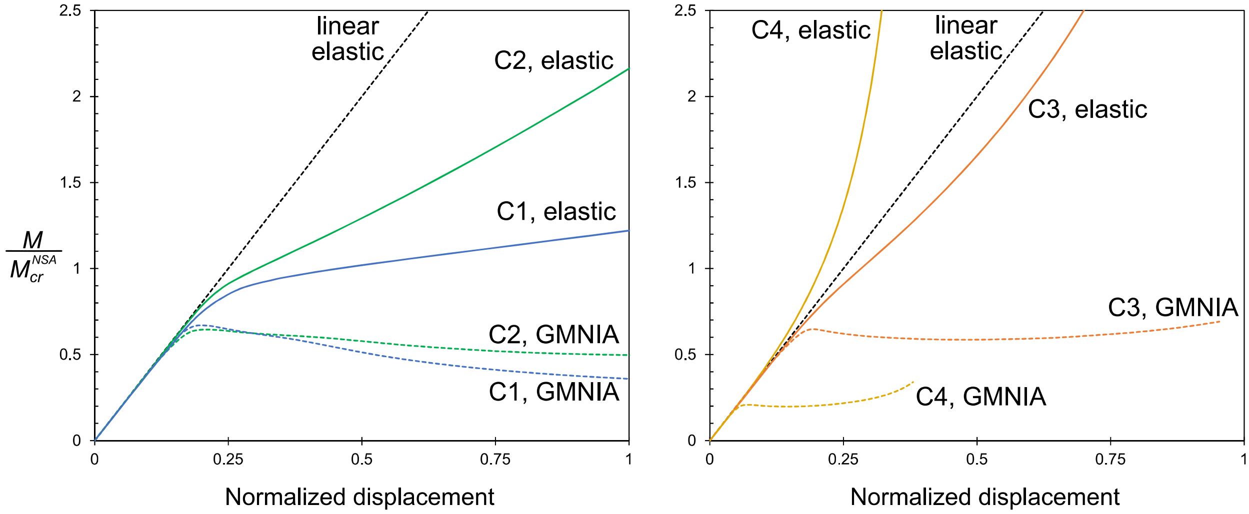

Figure 6: Uniaxial bending load-displacement plots for Case 3 and the beam lengths in Table 3

Table 3: Comparison between GMNIA and Eurocode 3 reduction factors for the uniaxial bending Case 3

Section	L (m)	β	$\bar{\lambda}_{LT}$	χ_{EC3}^{GC}	χ_{EC3}^{SC}	$\chi_{EC3,mod}^{GC}$	$\chi_{EC3,mod}^{SC}$	χ_{GMNIA}
C1	4	1.04	0.880	0.75	0.77	0.85	0.88	0.90
C2	10	1.28	0.986	0.68	0.71	0.76	0.80	0.85
C3	25	1.61	1.061	0.62	0.66	0.70	0.74	0.93
C4	25	4.33	0.944	0.70	0.73	0.80	0.83	1.00

Concerning the reduction factors provided in Table 3, it is concluded that, without the modification factor, the EC3 values are well below the GMNIA ones, even for the SC (about 15% for C1 and C2; 28% for C3 and C4). However, the differences are greatly reduced using the modification factor — 2.0, 6.0, 20 and 18% for C1 to C4, respectively —, showing that this method could be applied to cantilevers. Nevertheless, even with this factor, as in the previous cases, the C3 and C4 beams exhibit resistances far above those provided by Eurocode 3. In particular, beam C4 sustains increasing loads as the displacement increases (thus a reduction factor equal to 1.0 was considered), which is related to the fact that this beam exhibits a particularly high elastic post-buckling stiffness.

As in the previous cases, the buckling behavior of C3 and C4 section beams with varying length is investigated in detail. The left-side graphs in Fig. 7 show the variation of the GMNIA reduction factors with the slenderness and the corresponding normalized load-displacement curves are displayed in the right-side graphs in the figure. For the 12 m long C4 beam, a maximum load is not obtained and therefore the corresponding reduction factor is not shown in the left graph. These results lead to the following conclusions:

(i) The left-side graphs show that the GMNIA reduction factors are well above the EC3 buckling curves, as previously concluded from the results in Table 3. In comparison with the previous Cases 1 and 2, the present Case 3 exhibits the highest reduction factors, with most values falling above the Euler curve and very close to 1.0, namely for cross-section C4 (the one with the highest I_z/I_y ratio).

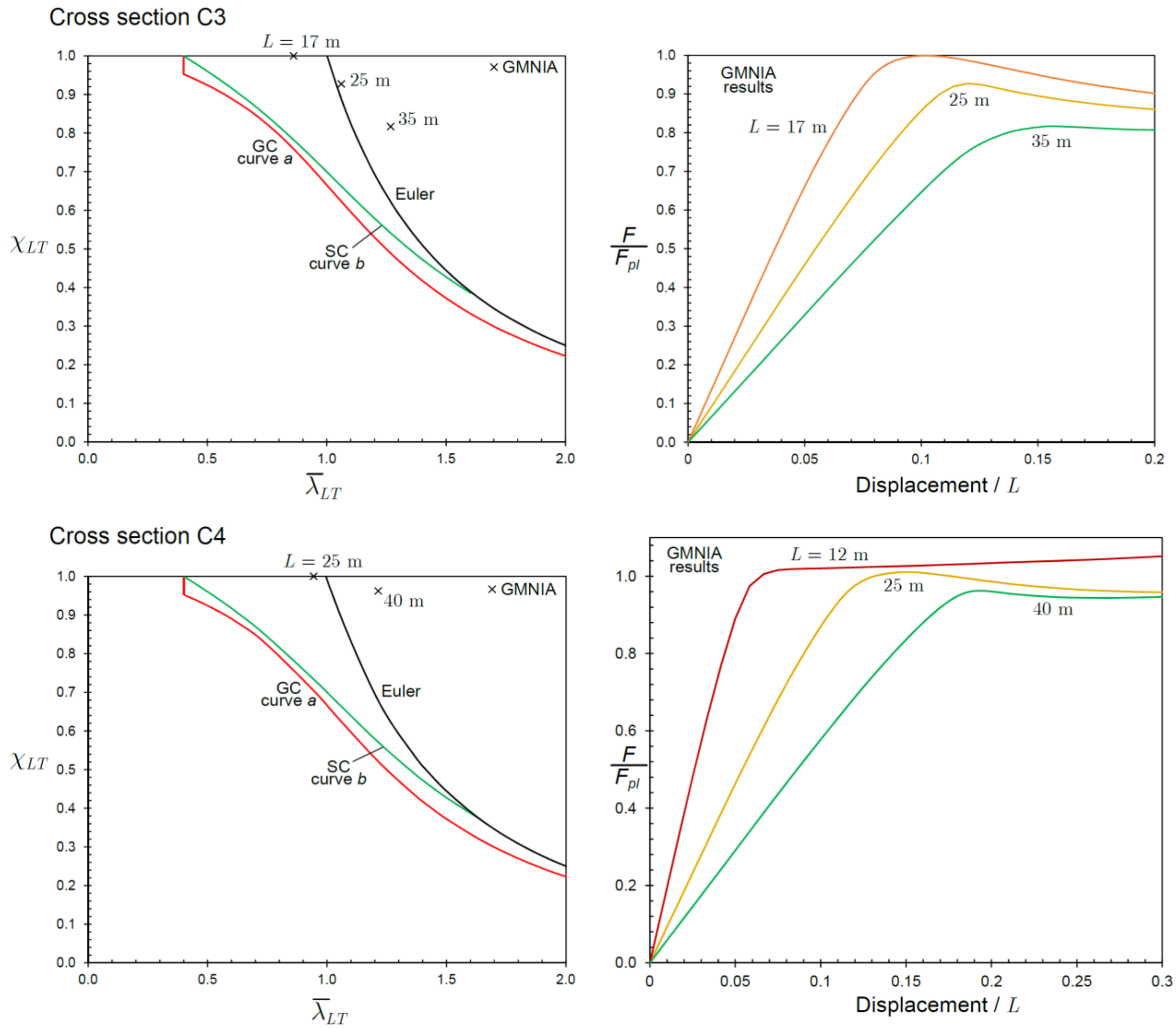

Figure 7: GMNIA results for the uniaxial bending Case 3 and C3-C4 sections with varying length: reduction factors as a function of the slenderness (left) and normalized load-displacement curves (right)

(ii) Although a very high load-carrying capacity is observed, the collapse loads are attained at very large normalized displacements (much higher than those in Figs. 3 and 5). For instance, for the C3 beam with $L = 35$ m, the GMNIA maximum load corresponds to a vertical displacement equal to $0.157L = L/6.36$ (see the top right graph in Fig. 7).

3. Lateral-torsional buckling under biaxial bending

Consider now beams subjected to biaxial bending and failing in LT buckling. In this case the EC3 beam-column interaction formulas must be employed to check the buckling ultimate limit state. Two methods are provided in the code, but only the so-called "Method 2" is analyzed in this paper, since it involves much simpler expressions. With this method, the interaction formulas for biaxial bending simplify to

$$\frac{C_{my} M_{y,Ed}}{\chi_{LT} M_{y,pl}} + \frac{0.6 C_{mz} M_{z,Ed}}{M_{z,pl}} \leq 1, \tag{3}$$

$$\frac{min\,(0.6+\bar{\lambda}_z;1)M_{y,Ed}}{\chi_{LT}M_{y,pl}}+\frac{C_{mz}M_{z,Ed}}{M_{z,pl}}\leq 1, \tag{4}$$

where $C_{my}, C_{mz} \leq 1.0$ are the so-called equivalent uniform moment factors, which depend on the shape of the corresponding moment diagram between relevant braced points, and $M_{pl} = M_{Rk}/\gamma_{M1}$. It is important to note that both formulas constitute linear interactions and that the second formula governs provided that $\bar{\lambda}_z > 0.4$ (which is verified in all cases considered in this paper) or that $C_{my} < 0.6 + \bar{\lambda}_z$ (if $\bar{\lambda}_z < 0.4$). In particular, provided that $\bar{\lambda}_z > 0.4$, the second formula yields a line that connects the points ($M_{y,Ed} = \chi_{LT}M_{y,pl}; M_{z,Ed} = 0$) and ($M_{y,Ed} = 0; M_{z,Ed} = M_{z,pl}/C_{mz}$). The second point lies outside the cross-section plastic resistance interaction curve if $C_{mz} < 1.0$ and, for this reason, the code specifies that such check is also required.

In order to assess the performance of the EC3 interaction formulas, the three loading/support cases shown in Fig. 8 are examined (although the support conditions are only displayed for the vertical plane, they also hold for the horizontal plane). Moreover, in Case 3, the forces are applied at the free end cross-section shear centre. The figure also shows the cross-section geometry adopted, which corresponds to a standard IPE 200 section without flange-web radii, as well as the material properties and the residual stress pattern. It should be noted that this cross-section has a height/width ratio equal to 2 and therefore lies precisely at the boundary between bucking curves *a*/*b* for the GC and *b/c* for the SC, with the higher (most favorable) curves in each case being prescribed by the code.

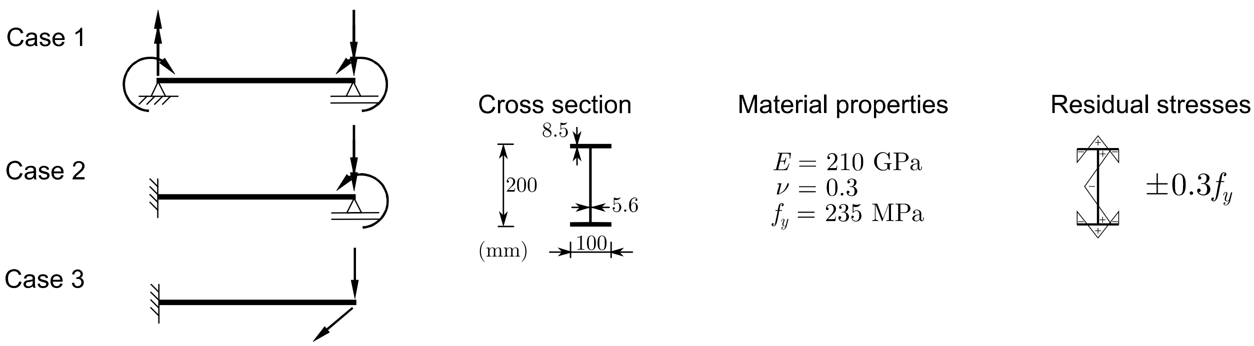

Figure 8: Support/loading cases, cross-section geometry, material properties and residual stresses considered for the biaxial bending analyses

First, Fig. 9 presents the GMNIA results for $M_{z,Ed} = 0$ (uniaxial bending) in the form of buckling curves, as a function of the slenderness $\bar{\lambda}_{LT}$, as well as the EC3 buckling curves (the curves obtained using the modification factor f are also presented for each case). These results prompt the following remarks:

(i) The GMNIA reduction factors for Case 1 fall slightly below the EC3 buckling curves, particularly the SC buckling curve and low-to-intermediate slenderness values. However, recall that hardening is not being considered and that this cross-section lies precisely in the border between buckling curves, with the most favorable one being prescribed by the code. Moreover, as already mentioned in Section 2.1, a similar behavior was reported by Taras & Greiner (2010) for an IPE500 beam, namely when compared with the SC.

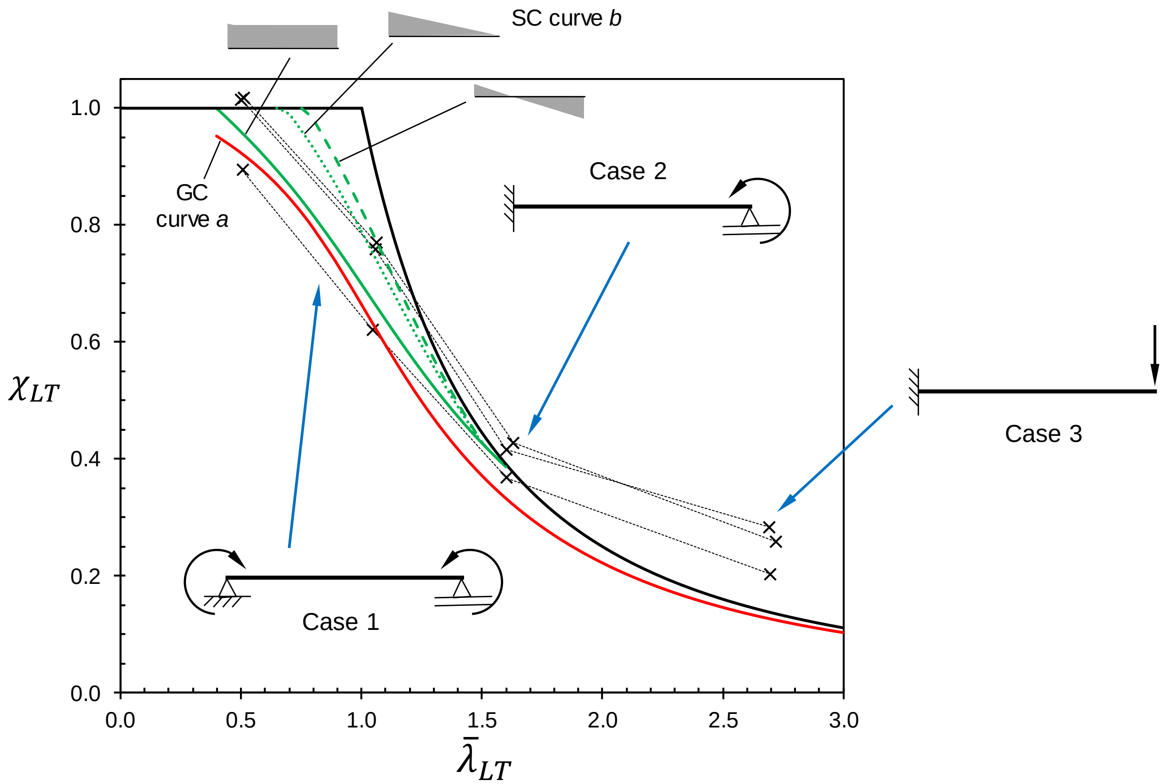

Figure 9: GMNIA results for uniaxial bending ($M_z = 0$), for the cases in Fig. 8

(ii) The GMNIA results for Cases 2 and 3 fall significantly above the GC curve, but fit rather well with the corresponding SC curves. This shows once more that the modification factor could be applied to the cantilever case (Case 3).

(iii) In accordance with the results presented in the previous Section, the GMNIA reduction factors fall above the Euler curve for high slenderness values and this behavior is more pronounced for the cantilever case (Case 3). However, it is observed that the GMNIA results for Case 2 are very similar to those of the cantilever, most probably due to its statically indeterminacy. In these cases serviceability would be the governing limit state.

Next, the biaxial bending for each Case is analyzed in detail. Figs. 10-12 display the normalized $m_y - m_z$ interaction diagrams (with $m_i = M_{i,Ed}/M_{i,pl}$) for four slenderness values, obtained from (i) GMNIA analyses, (ii) the interaction formula (4), using for the reduction factor χ_{LT} the values obtained from the GMNIA analysis with $M_{z,Ed} = 0$, and (iii) the exact cross-section plastic resistance, calculated from the analytical formulas developed by Baptista (2012). Moreover, for the slenderness value cases where the reduction factor lies above the Euler curve, a horizontal line corresponding to $\chi_{LT} = 1/\bar{\lambda}_{LT}^2$ (hence $M_{y,Ed} = M_{cr}$) is provided in the graphs. These interaction diagrams are calculated for reference moments given by $\bar{M}_y = M_{y,pl} \sin\theta$ and $\bar{M}_z = M_{z,pl} \cos\theta$, with θ = {90º, 79º, 67.5º, 45º, 22.5º, 11º, 0º}. For each reference moment pair, the maximum loading is therefore given by $M_{y,Ed} = \Lambda\bar{M}_y = \Lambda M_{y,pl} \sin\theta$ and $M_{z,Ed} = \Lambda\bar{M}_z = \Lambda M_{z,pl} \cos\theta$, where Λ is the maximum load parameter, obtained from GMNIAs, the EC3 formulas or the cross-section resistance. This means that the maximum normalized moments are given by $m_y = \Lambda \sin\theta$ and $m_z = \Lambda \cos\theta$, hence $\tan\theta = m_y/m_z$.

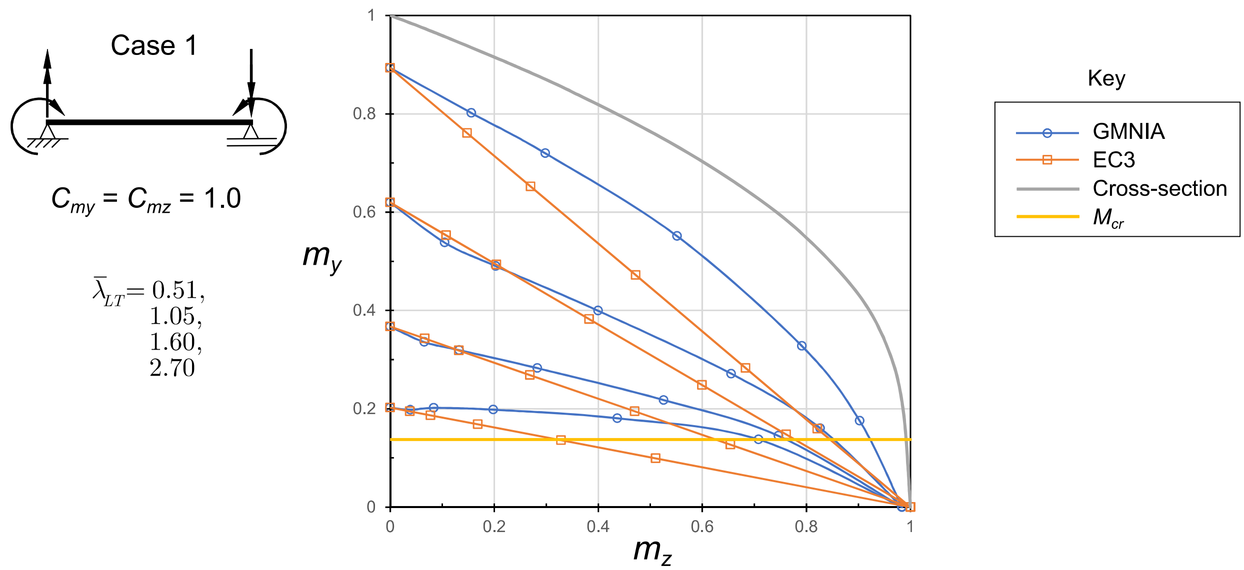

Figure 10: $m_y - m_z$ interaction diagrams for Case 1

The interaction diagram for Case 1 is presented in Fig. 10 and leads to the following conclusions:

(i) The GMNIA curves exhibit significant "inward" curvatures. This contrasts with the outward curvature generally found in the interaction diagrams of members subjected axial force and bending moment (see, e.g., Gonçalves & Camotim 2004). However, it is also worth noting that, for the intermediate slenderness values (1.05 and 1.60) and $\theta = 79°$, the GMNIA curves show a slight "outward" curvature.

(ii) The Eurocode 3 Method 2 formulas yield straight lines and thus, generally, very conservative results. Recalling Fig. 9, if the GC was used instead to obtain χ_{LT} (buckling curve *a*), the results would turn out slightly more conservative, except for $\bar{\lambda}_{LT} = 0.51$, in which case the GMNIA result falls below the buckling curves. With the SC (buckling curve *b*), a better fit of the GMNIA results would be obtained.

(iii) For the most slender beam ($\bar{\lambda}_{LT} = 2.70$), all GMNIA results fall above the M_{cr} horizontal line except for $\theta = 0°$ (which corresponds to $m_y = 0$). This means that, for this case and $\theta \geq 11°$, one could use $\chi_{LT} = 1/\bar{\lambda}_{LT}^2$ and ignore $M_{z,Ed}$.

For Case 2, two interaction diagrams are displayed in Fig. 11, which differ only in the C_m factors used in Eqs. (3)-(4): (i) while the left side diagram was obtained with the values prescribed by Eurocode 3 for the M_y and M_z bending moment diagrams shapes (in this case $C_{my} = C_{mz} = 0.4$), (ii) the right side one corresponds to $C_{my} = C_{mz} = 0.75$, which is the value recommended by Gonçalves & Camotim (2004) for the in-plane case with $N + M_y$ and this loading/boundary conditions. These results prompt the following remarks:

(i) As in the previous case, the GMNIA curves exhibit significant inward curvatures and, for the intermediate slenderness value ($\bar{\lambda}_{LT} = 1.06$) and $\theta = 79°$, a slight outward curvature is observed. It is also worth noting that, for the same slenderness, all the GMNIA curves for Case 2 are higher than for Case 1, *i.e.*, Case 2 exhibits a higher resistance with respect to Case 1. For instance, for $\bar{\lambda}_{LT} = 0.51$, the GMNIA curve in Fig. 11 (both graphs, obviously)

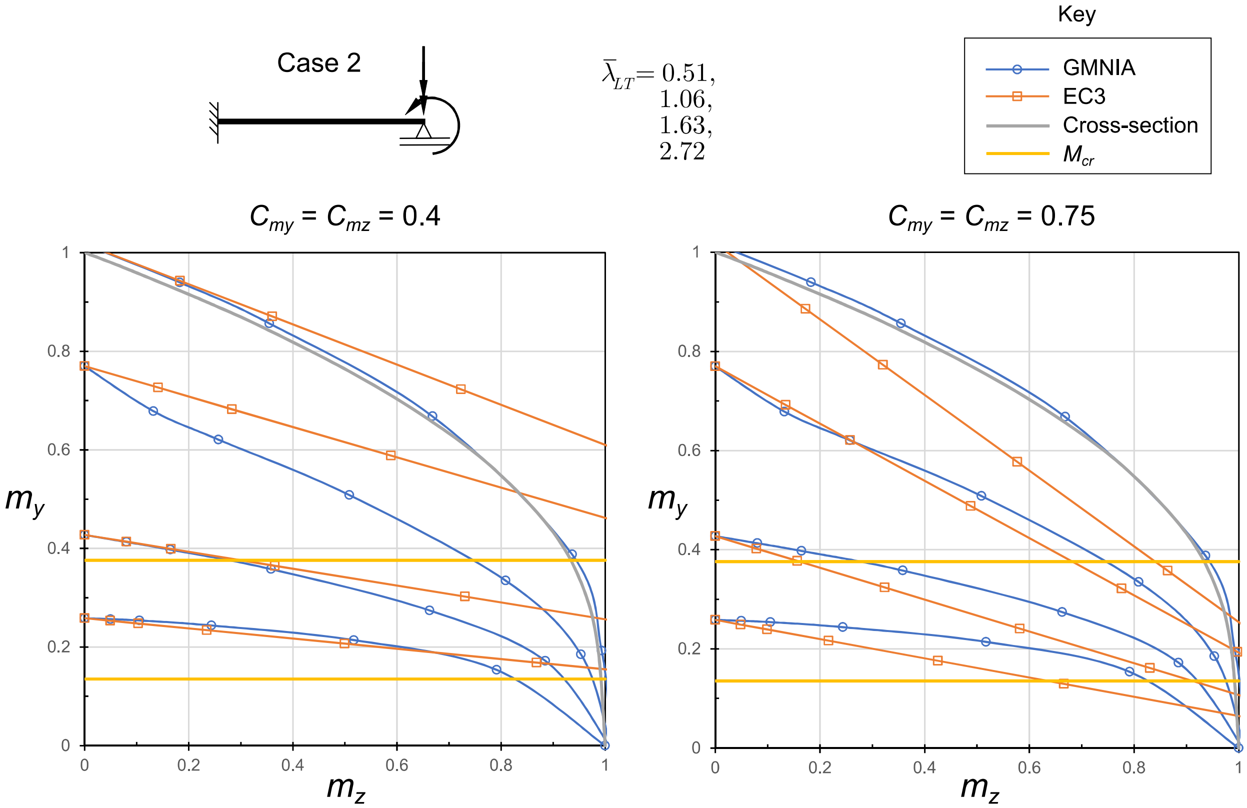

Figure 11: $m_y - m_z$ interaction diagrams for Case 2

coincides with the cross-section interaction, whereas the corresponding GMNIA curve in Fig. 10 falls significantly below the cross-section interaction.

(ii) As previously pointed out, the Eurocode 3 formulas yield straight lines. For the left graphs, this leads to unconservative results, in accordance with what was pointed out by Gonçalves & Camotim (2004) for the $N + M_y$ in-plane case. With $C_{my} = C_{mz} = 0.75$ (right graphs), much better results are obtained, although excessively on the conservative side in some cases. If the GC curve a was used instead to obtain χ_{LT}, the EC3 interaction curves would be much lower than those shown in the diagrams. However, this is not the case if the SC modified curve b was employed — recall from Fig. 9 that the GMNIA results for Case 2 fall well above the GC curve but fit rather well with the SC modified curve, except for the highest slenderness.

(iii) For $\bar{\lambda}_{LT} = 1.63, 2.72$, some GMNIA results lie above the M_{cr} horizontal line, most notably for the latter case where, for $\theta \geq 11°$, if $\chi_{LT} = 1/\bar{\lambda}_{LT}^2$ would be used, the effect of $M_{z,Ed}$ could be discarded.

Finally, Fig. 12 shows the results for Case 3, where Eqs. (3)-(4) are computed with $C_{my} = C_{mz} = 0.9$, in accordance with EC3. These results lead to the following conclusions:

(i) Once again, the GMNIA curves exhibit significant inward curvatures, except for $\bar{\lambda}_{LT} = 1.06$ and $\theta = 79°$, where a slight outward curvature is again observed. For $\bar{\lambda}_{LT} = 0.50$ the GMNIA curve falls outside the cross-section interaction, due to the occurrence of large displacements which lower the moments at the built-in end (recall from Fig. 9 that, for this slenderness, the reduction factor falls above the horizontal plateau).

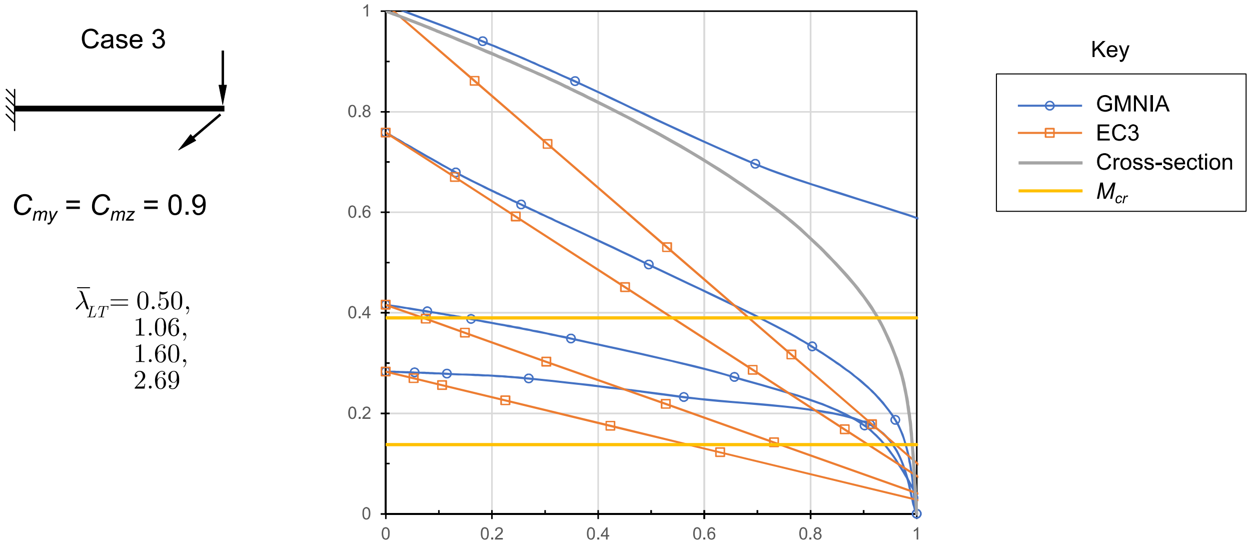

Figure 12: $m_y - m_z$ interaction diagrams for Case 3

(ii) Once more, the Eurocode 3 formulas yield straight lines which are very on the conservative side and, if the buckling curves were used instead to obtain χ_{LT}, much more conservative results would be obtained (recall Fig. 9). Using the GC curve *a* to obtain χ_{LT} would lead to much lower EC3 interaction curves, but the SC modified curve *b* would produce interaction curves similar to those in Fig. 12 — recall from Fig. 9 that the GMNIA results for Case 3 fall well above the GC curve but fit rather well with the SC modified curve, except for the highest slenderness.

(iii) For the $\bar{\lambda}_{LT} = 2.69$ beams, most GMNIA results lie above the M_{cr} horizontal line and, again, for these cases if $\chi_{LT} = 1/\bar{\lambda}_{LT}^2$ would be used, the contribution of $M_{z,Ed}$ could be ignored.

4. Concluding remarks

This paper presented and discussed results concerning the application of the current Eurocode 3 provisions for compact I-section beams undergoing lateral-torsional buckling and subjected to uniaxial and biaxial bending. In particular, the Eurocode 3 formulas were compared with GMNIA (geometrically and materially non-linear numerical analyses, including geometric imperfections and residual stresses) results obtained using a geometrically exact beam finite element. This element is capable of handling Wagner effects, plasticity, geometric imperfections and residual stresses.

For the uniaxial bending case, besides I-sections with standard height-to-width ratios, wider flange sections were analyzed and three support/loading cases were considered: (Case 1) simply supported beams under uniform moment, (Case 2) simply supported beams subjected to a mid-span vertical force and (Case 3) cantilevers subjected to a free end vertical force. The following conclusions should be highlighted:

(i) For all cases, the elastic post-bucking equilibrium paths are very stable.

(ii) As the I_z/I_y ratio increases (but $I_z/I_y < 1$), the critical buckling moment accounting for pre-buckling deflections becomes increasingly higher than that obtained from a linear stability analysis. For the cases considered in this paper, this increase can be estimated using the β parameter given by Eq. (2), even though it was developed for Case 1. It was also shown that, as I_z/I_y increases, the elastic post-buckling paths become stiffer, particularly for cantilevers (Case 3).

(iii) The GMNIA post-critical path is also related to the I_z/I_y ratio — as this ratio increases, the slope of the post-critical path also increases, with the wide flange sections exhibiting the less negative slopes (sometimes positive).

(iv) A comparison between the GMNIA and the Eurocode 3 buckling resistance values showed that, as expected, for the cross-sections with standard height-to-width ratios, the code provides accurate resistance values except for Case 3, in which case rather conservative values are obtained (but can be minimized using the modification factor). For the cross-sections with high I_z/I_y ratios, the GMNIA results generally fall well above the Eurocode 3 values, due to their high post-buckling stiffness. However, these cases are most likely governed by the serviceability limit state.

For the biaxial bending case, a standard IPE 200 section was considered and three support/loading cases were examined: (Case 1) simply supported beams under uniform moments, (Case 2) beams simply supported at one end and fixed at the other, subjected to end moments, and (Case 3) cantilevers subjected to free end forces. It was demonstrated that the Eurocode 3 Method 2 provisions can lead to very inaccurate estimates of the collapse loads, which can be either on the conservative or unconservative side. It is also worth remarking that, for high slenderness values, the GMNIA ultimate load is significantly above the critical bifurcation load, due to the fact that large displacements are involved (again, serviceability is likely to govern). In these cases, if $\chi_{LT} = 1/\bar{\lambda}_{LT}^2$ is employed, the contribution of $M_{z,Ed}$ could be ignored.

References

Atluri, S., Iura, M., Vasudevan, S. (2001). "A consistent theory of finite stretches and finite rotations, in space-curved beams of arbitrary cross-section." Computational Mechanics 27 (4) 271-281.

CEN (2005). *EN 1993-1-1 Eurocode 3: Design of steel structures – Part 1-1: General rules and rules for buildings*. Brussels: CEN.

Baptista, A. (2012). "Resistance of steel I-sections under axial force and biaxial bending." *Journal of Constructional Steel Research*, 72 1-11.

Gonçalves, R., Camotim, D. (2004). "On the application of beam-column interaction formulae to steel members with arbitrary loading and support conditions." *Journal of Constructional Steel Research*, 60 (3-5) 433-450.

Gonçalves, R., Ritto-Corrêa, M., Camotim, D. (2010). "A large displacement and finite rotation thin-walled beam formulation including cross-section deformation." *Computer Methods in Applied Mechanics and Engineering*, 199 (23-24) 1627-1643.

Gonçalves, R. (2016). "A shell-like stress resultant approach for elastoplastic geometrically exact thin-walled beam finite elements." *Thin-Walled Structures* 103 263-272.

Gonçalves, R. (2019). "An assessment of the lateral-torsional buckling and post-buckling behaviour of steel I-section beams using a geometrically exact beam finite element." *Thin-Walled Structures* 143 106222 (15 pages).

Gruttmann, F., Sauer, R., Wagner, W. (2000). "Theory and numerics of three-dimensional beams with elastoplastic material behavior." *International Journal for Numerical Methods in Engineering*, 48 1675-1702.

Kucukler, M., Gardner, L., Macorini, L. (2015). "Lateral–torsional buckling assessment of steel beams through a stiffness reduction method." *Journal of Constructional Steel Research* 109 87-100.

MATLAB (2010), version 7.10.0 (R2010a), *The MathWorks Inc.*, Massachusetts.

Pi, Y., Trahair, N. (1992). "Prebuckling deflections and lateral buckling. II: Applications." *Journal of Structural Engineering*, 118 (11) 2967-2985.

Rebelo, C., Lopes, N., Simões da Silva, L., Nethercot, D., Vila-Real, P. (2009). "Statistical evaluation of the lateral-torsional buckling resistance of steel I-beams, part 1: Variability of the Eurocode 3 resistance model." *Journal of Constructional Steel Research*, 65 (4) 818-831.

Reissner, E. (1972). "On one-dimensional finite-strain beam theory: the plane problem." *Journal of Applied Mathematics and Physics (ZAMP)*, 23 795-804.

Simo, J. (1985). "A finite strain beam formulation. The three-dimensional dynamic problem, Part I." *Computer Methods in Applied Mechanics and Engineering*, 49 55-70.

Simo, J., Vu-Quoc, L., (1991). "A geometrically-exact rod model incorporating shear and torsion-warping deformation." *International Journal of Solids and Structures*, 27 (3) 371-393.

Snijder, H., Hoenderkamp, J. (2007). "Buckling curves for lateral torsional buckling of unrestrained beams." *Proceedings of the Hommages à René Maquoi Birthday Anniversary*, Belgium, Université de Liège, 239-248.

Snijder, H., Hoenderkamp, J., Bakker, M., Steenbergen, H., de Louw, C. (2008). "Design rules for lateral torsional buckling of channel sections subject to web loading." *Stahlbau* 77 (4) 247-256.

Snijder, H., van der Aa, R., Hofmeyer, H., van Hove, B. (2018). "Lateral torsional buckling design imperfections for use in non-linear FEA." *Steel Construction* 11 (1) 49-56.

Taras, A. (2016). "Derivation of DSM-type resistance functions for in-plane global buckling of steel beam-columns." *Journal of Constructional Steel Research*, 125 95-113.

Taras, A., Greiner, R. (2008). "Development of consistent buckling curves for torsional and lateral-torsional buckling." *Steel Construction* 1 (1) 42-50.

Taras, A., Greiner, R., (2010). "New design curves for lateral-torsional buckling. Proposal based on a consistent derivation." *Journal of Constructional Steel Research*, 66 (5) 648-663.